LASER INTERFEROMETER GRAVITATIONAL WAVE OBSERVATORY
- LIGO -
CALIFORNIA INSTITUTE OF TECHNOLOGY
MASSACHUSETTS INSTITUTE OF TECHNOLOGY

Technical Note **LIGO-T2600282v1-G** 09/13/2026

2026 LIGO SURF Final Report: Active Magnetic Field Stabilization for Cold-Atom Precision Measurement

Martin Zanazzi[1], Jeffrey Wack[2], Lee McCuller[2]
[1] *Utah Valley University,* [2] *California Institute of Technology*

California Institute of Technology
LIGO Project, MS 18-34
Pasadena, CA 91125
Phone (626) 395-2129
Fax (626) 304-9834
E-mail: info@ligo.caltech.edu

Massachusetts Institute of Technology
LIGO Project, Room NW17-161
Cambridge, MA 02139
Phone (617) 253-4824
Fax (617) 253-7014
E-mail: info@ligo.mit.edu

LIGO Hanford Observatory
Route 10, Mile Marker 2
Richland, WA 99352
Phone (509) 372-8106
Fax (509) 372-8137
E-mail: info@ligo.caltech.edu

LIGO Livingston Observatory
19100 LIGO Lane
Livingston, LA 70754
Phone (225) 686-3100
Fax (225) 686-7189
E-mail: info@ligo.caltech.edu

http://www.ligo.caltech.edu/

Abstract

The Rubidium Quantum Sensing (RbQ) experiment transfers optical signals into rubidium-87 hyperfine populations for selective single-photon detection, in eventual support of GQuEST. ^{87}Rb hyperfine coherence is sensitive to ambient magnetic field noise, which induces Zeeman-effect decoherence. Because conventional mu-metal shielding is difficult to reconcile with the experiment's vacuum, space, and bias field constraints, this project develops a supplemental active magnetic field stabilization system targeting the lab's dominant 60 Hz noise and harmonics. A compact 3-axis Helmholtz-coil apparatus was built to validate the sensing and feedback architecture, suppressing field variations down to a sensor-limited noise floor of $4\,\mathrm{nT}/\sqrt{\mathrm{Hz}}$ at 1 Hz. Work began by characterizing and comparing candidate magnetic sensors and readout electronics, including an anisotropic magnetoresistive sensor that requires periodic high-current reset pulses and a tunneling magnetoresistive sensor with a modestly higher noise floor but no reset requirement. Several instrumentation amplifiers were also tested in parallel, with the design ultimately settling on the tunneling magnetoresistive sensor for its simplicity paired with a differential output instrument amplifier. These findings informed the design, components, simulation, and fabrication of three custom PCBs (sensor, signal-conditioning, and coil-driver boards) implementing the full feedback loop. Preliminary P-loop results with custom frequency-dependent gain filters suppressed ambient lab noise by 22, 19, and 20 dB at 60, 180, and 300 Hz, respectively.

1 Introduction

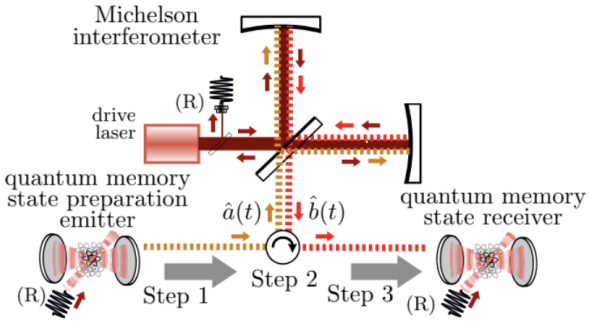


Figure 1: Overview of the RbQ system with Michelson interferometer, adapted from [1].

The Rubidium Quantum Sensing project (RbQ) aims to transfer weak optical signals into hyperfine state populations in rubidium-87 atoms, enabling single-photon detection selective to specific frequencies and temporal modes [1–3]. As shown in Fig. 1, rubidium-87 atoms are laser cooled using a three-dimensional magneto-optical trap (3DMOT). Driving the system with a control laser stimulates a two-photon Raman process that drives the transition through an intermediate excited state [4] (Fig. 2). A direct transition between these two states is forbidden by electric dipole selection rules, so the transition can only occur via this two-photon process, which requires the combined action of the signal photon and control laser photon. After this transition, the atoms can be put through a process that causes significant

fluorescence, enabling simple readout. By tuning the control laser's parameters, the system can be designed so that only signal photons of very specific frequencies and temporal modes trigger the two-stage transition.

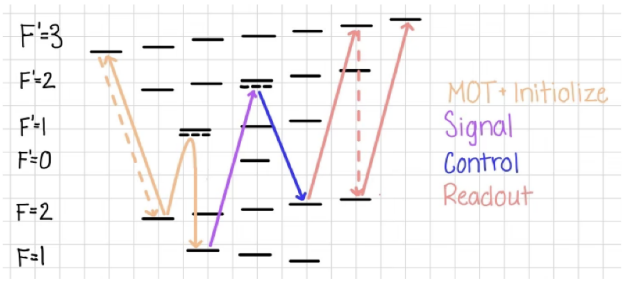


Figure 2: Atomic transitions involved in the RbQ experiment [4].

This system will serve as a testbed for future cold-atom sensing applications with a particular emphasis on applications typically reserved for Superconducting Nanowire Single Photon Detectors (SNSPDs). Specifically, RbQ is poised to be integrated into the GQuEST experiment, where it will be tasked with detecting and characterizing signal photons from a dual tabletop interferometer [5]. This system provides access to measurements beyond those achievable through conventional optical detection alone and will serve as a proof of concept for integration into larger projects.

The nature of the high-precision measurements in RbQ and other atomic physics experiments often requires a highly stable and controlled magnetic field typically achieved through mu-metal passive shielding. However, space constraints, ease of access, bias field requirements, and vacuum compatibility have led to the evaluation of active stabilization. In cold atom systems, magnetic field fluctuations can shift atomic transition frequencies through the Zeeman effect, leading to phase decoherence and measurement degradation [6]. Because many quantum and atom-light interactions rely on maintaining coherent hyperfine states, environmental magnetic noise becomes a major limitation to experimental sensitivity and stability. In lab environments, 60 Hz magnetic noise and its associated harmonics from surrounding electrical systems are particularly problematic. Active magnetic field stabilization provides a controllable suppression method that is especially effective for low-frequency environmental noise.

This project's goal was to construct a proof-of-principle apparatus for active magnetic field stabilization that could be 3D printed for easy assembly and testing, primarily aimed at eliminating the dominant 60 Hz noise in the lab and any related harmonics. The target performance of this system required reducing the noise level at a central point to where it is limited only by the specifications of the chosen magnetoresistive sensors, in this case 4 nT $\mathrm{Hz}^{-1/2}$. Finally, the system must be capable of holding both a nonzero and zero magnetic field with arbitrary directionality.

2 Methods

2.1 Initial Sensor Characterization

The first phase of the project focused on characterizing the capabilities and noise floor of the Honeywell 1051Z Anisotropic Magnetoresistive (AMR) sensor and the NVE ALT021 Tunneling Magnetoresistive (TMR) sensor. Additionally, I focused on determining the ideal complete circuit for each sensor, prioritizing low voltage noise and simplicity.

2.2 Honeywell 1051Z Sensor Characteristics

The 1051Z is an AMR single-axis sensor promising a noise floor of 1 nT $\mathrm{Hz}^{-1/2}$ and a sensitivity of 1 mV/V/G [7]. Because the data sheet specifies noise as a voltage density, this noise floor was calculated using a 10 V bridge voltage and the specified sensitivity. Work on characterizing this sensor used a breadboard test circuit (Fig. 3) and a 3D printed coil (Fig. 4), and included experimental sensitivity measurements (Fig. 5), swept sines (Fig. 6), and noise floor measurements.

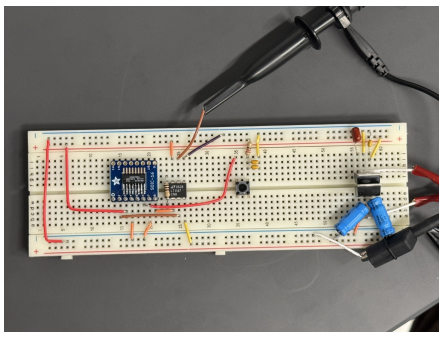


Figure 3: 1051Z test circuit.

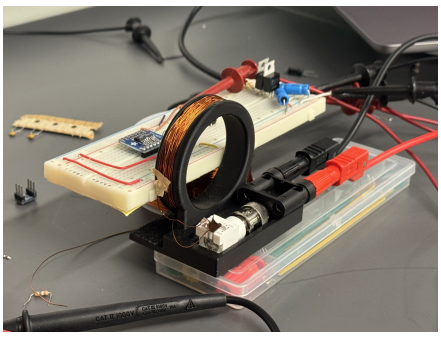


Figure 4: Sensitivity testing with 3D printed coil.

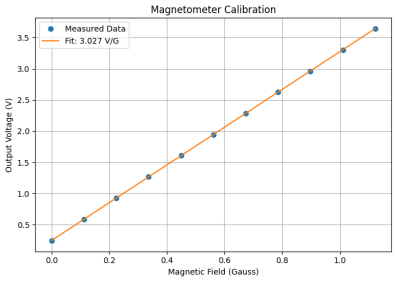


Figure 5: 1051Z sensitivity results. Dividing the linear fit slope by the amplifier gain and supply voltage gives 1.196 mV/V/G, which is within the specified range of 0.8–1.2 mV/V/G given in the data sheet.

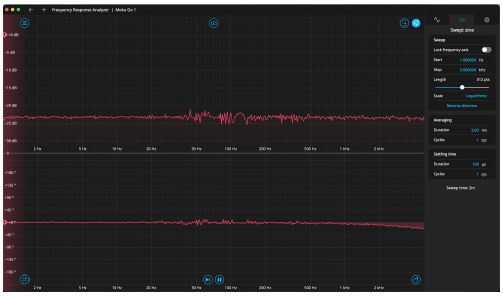


Figure 6: A swept sine measurement of the 1051Z. The measurement remains relatively stable except for noise between 50 and 100 Hz, as expected, and a slight phase delay between 2 and 5 kHz.

Noise floor measurements were fraught with issues. Notably, it is difficult to differentiate between electrical noise, sensor noise, and ambient magnetic fields. I showed that the use of a breadboard, while convenient, introduces significant noise on its own, on the order of hundreds of nVrms/Hz$^{1/2}$. Moving to a soldered circuit would reduce this noise, but first required identifying a suitable instrumentation amplifier and supporting components. Because the 1051Z was ultimately not selected for the final design, a final noise floor measurement of the sensor was not completed. However, the data sheet specifications give a noise floor of $1\,\mathrm{nT}/\sqrt{\mathrm{Hz}}$ at 1 Hz, and the evidence gathered up until that point suggested this value was correct.

The performance of the 1051Z was satisfactory for this application. However, a major downside of the sensor is the requirement of a set/reset (SR) pulse. This pulse is required periodically to reset the magnetic domains within the sensor to maintain optimal sensitivity and reliability. Unfortunately, executing an SR pulse requires two closely spaced microsecond pulses of at least 500 mA [7]. Incorporating this in the final design would have added significant complexity and additional circuitry.

2.3 NVE ALT021 Sensor Characteristics

The ALT021 is a high-sensitivity TMR sensor housed in a small DFN6 surface-mount package. Notable characteristics of this sensor include a sensitivity rating of 500 mV/V/mT, 50 times higher than the 1051Z [8]. While it does have a specified noise floor about 4 times higher than the 1051Z, it does not require the use of an SR pulse to maintain sensitivity.

At the time of these initial tests, the sensors had only recently arrived in the lab, and as a result, I had limited time to thoroughly test their specifications. However, I carried out sensitivity measurements on both ALT021 sensors that were in the lab at the time (Fig. 7 and Fig. 8).

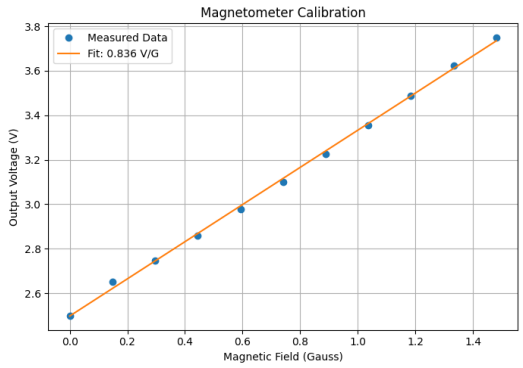


Figure 7: Sensor 1 sensitivity results. This sensor was about 3 times less sensitive than expected, with a value of 167 mV/V/mT.

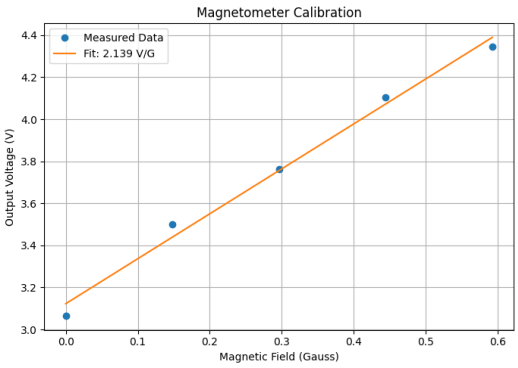


Figure 8: Sensor 2 sensitivity results. This sensor fell within specification with a sensitivity value of 428 mV/V/mT.

The factors likely at play in the significant difference in sensitivity were heat damage from soldering and imperfect solder joints (Fig. 9).

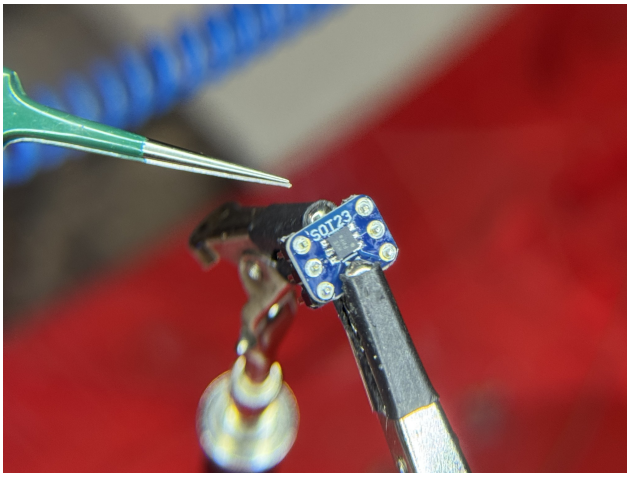


Figure 9: The small size of the DFN6 package resulted in initial difficulties in achieving stable solder joints to the breakout board. The additional heat used to fix imperfect joints may have caused internal heat damage to the sensor's Wheatstone bridge.

2.4 Instrumentation Amplifier Selection

The choice of amplifier used to read the voltage differential across each sensor's Wheatstone bridge has large effects on the capabilities of the final system. A low noise floor is vital; additionally, ease of use and form factor play a role as well. The two instrumentation amplifiers tested were the LT1167 and INA849. The LT1167 was the highest-performance amplifier available in the lab, and the INA849 was ordered as a lower-noise alternative.

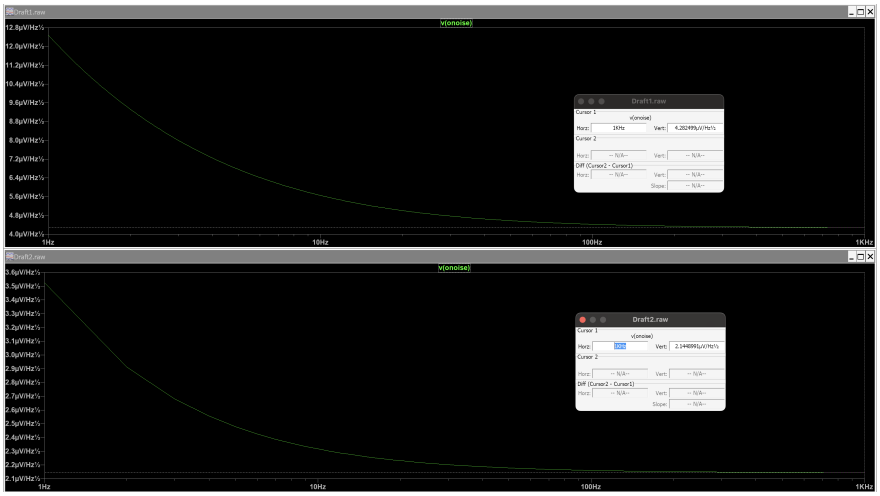


Figure 10: The INA849 proved to have a superior noise floor as compared to the LT1167 in LTspice simulations. These circuits were constructed with a resistor across the inputs of each amplifier intended to simulate the inherent noise of a sensor's Wheatstone bridge in a zero-field environment.

Experimental noise measurements throughout this phase of the project were taken with an SR785 signal analyzer (Fig. 11). Recreating the same simulated circuits (Fig. 10) and measuring the resulting noise yielded noise floor measurements 2.2 and 2.7 times higher for the LT1167 and INA849, respectively. I attributed this discrepancy to electrical noise from the breadboard and power supply.

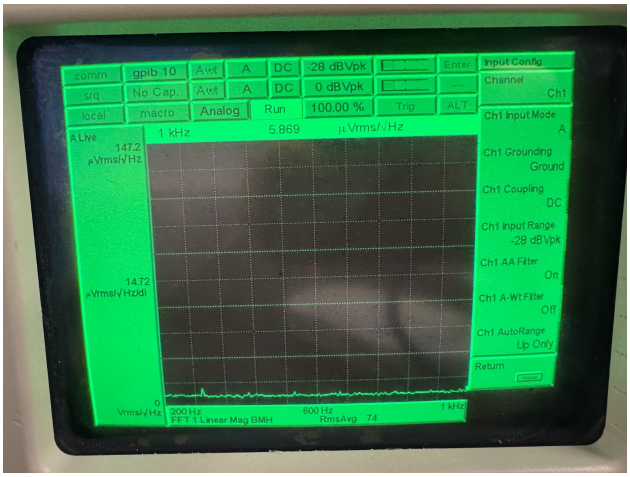


Figure 11: An example of a noise floor measurement on the SR785. Here, I was determining the LT1167's noise floor with shorted inputs on a breadboard.

During the final phase of PCB design, it was determined that a differential output was preferred over the single-ended output offered by both amplifiers tested. As a result, the TI INA851 was selected for final fabrication of the circuit. This amplifier offered similar low-noise performance with a fully differential output, ideal for the CyMAC ADC (the lab's

feedback and controls computer) [9].

2.5 Electronics Design

Three separate PCBs were designed: a sensor board, signal board, and coil driver board (Fig. 12). Each board was designed with precision analog measurement in mind, and ultra-low noise components were given priority. The signal is initially obtained on the sensor board before traveling through the signal board to the lab's feedback computer (CyMAC). The output from the computer is sent to the coil driver boards, which convert the command voltage to a current through an individual coil. While the six channels each have individual feedback control, they are arranged in Helmholtz pairs to maximize the field uniformity in the center of the apparatus. The sensor boards are connected to the signal boards with Molex Picoblade six-pin connectors, and the signals to and from the controls computer are sent via DE-9 cables. All boards run on an external ±12V source, which throughout testing was provided by a Rigol DP832A. While the model did not allow for negative voltage, I was able to create ±12V by setting two channels to +12V, then shorting the negative of channel 1 to the positive of channel 2 and designating that portion of the circuit ground.

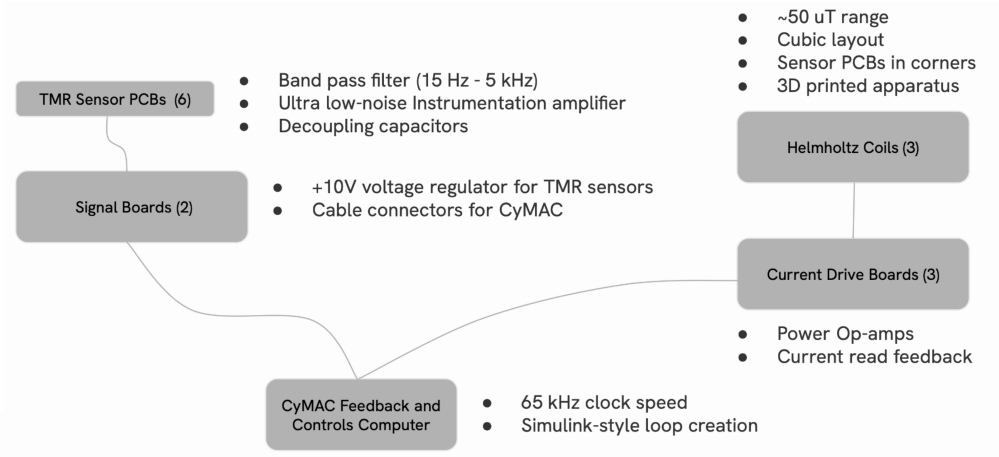


Figure 12: Circuitry overview of the active feedback mechanism.

2.6 Tunneling Magnetoresistive (TMR) Sensor PCBs

This board consists of an NVE ALT021-10E TMR sensor, a TI INA851 differential output instrumentation amp with gain set to 40, decoupling capacitors, and high/low pass filters to whiten the noise floor for high-resolution ADC conversion (Fig. 15). The corner of the high pass filter is around 15 Hz (Fig. 16) and designed to whiten the 1/f flicker noise floor of the TMR sensor. The low pass corner is situated at 7 kHz and tasked with removing high frequency noise that is beyond the capability of the Helmholtz coils. The board (Fig. 13) takes in ±12V, +10V, and GND via four of the Picoblade connector's six pins; the remaining two are reserved for the differential output of the INA851.

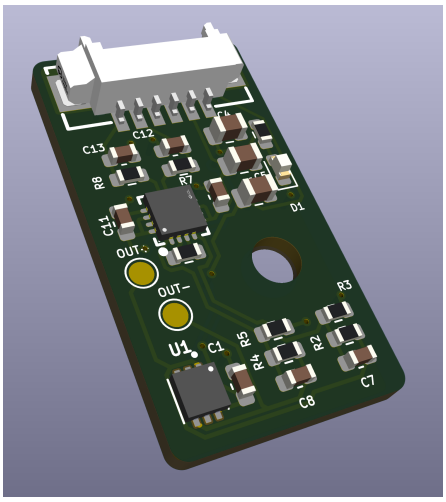


Figure 13: A render of the complete sensor board. The TMR sensor is located at the bottom left corner of the board.

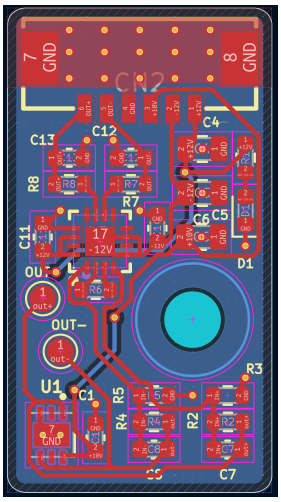


Figure 14: PCB design of the sensor board. Note the M3 mounting hole and test points for the unamplified differential output of the ALT021.

For simplicity, a two-layer board was chosen for this design (Fig. 14), with the bottom layer designated ground. Care was taken to ensure a low-impedance ground, with only vital traces routed through the bottom layer. A filled ground plane underneath the connector was included to create a solid connection between the cable and board ground, and a single M3 hole was included for mounting purposes.

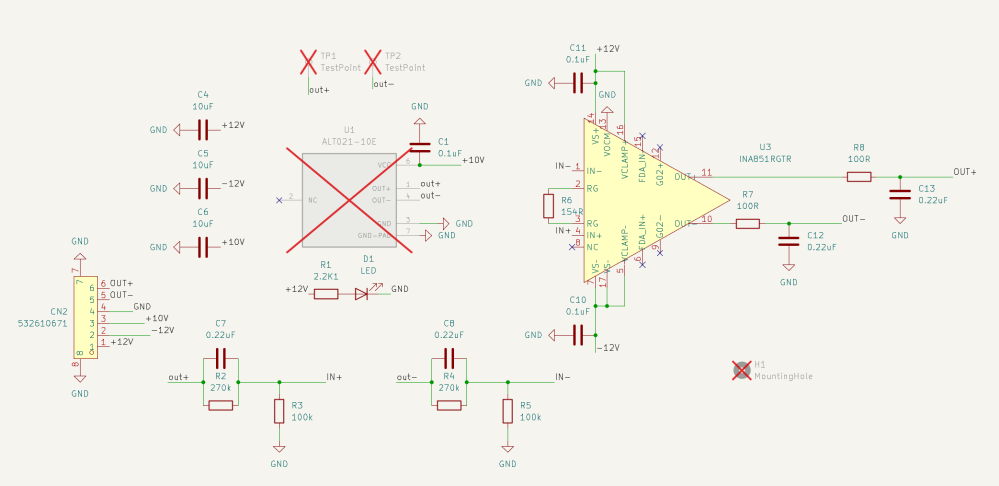


Figure 15: Sensor board schematic. The TMR sensor is crossed out as it is marked Do Not Place (DNP) as our PCB manufacturer, JLCPCB, did not have the part in stock.

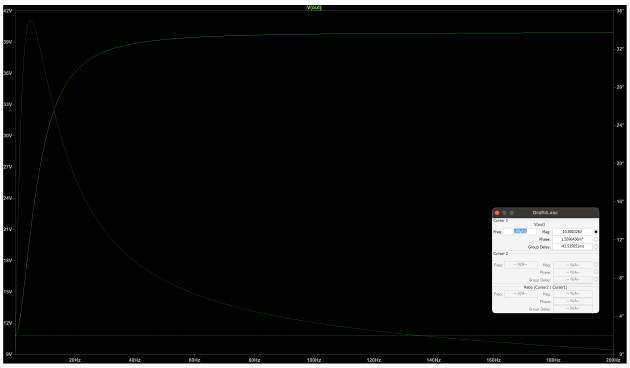


Figure 16: A simulation of a swept sine measurement on the high pass filters. Placing this filter before the amplifier ensures that no flicker noise is unnecessarily amplified, ultimately improving the ADC's resolution at low frequencies by decreasing the bin size.

2.7 Signal Board PCBs

These boards (Fig. 17) are designed to provide both the ±12V and +10V references required by the sensor boards and send the sensor differential signals into DE-9 ports to connect to the CyMAC. The +10V reference is provided by an LT3042 linear regulator (Fig. 19) and the ±12V references are provided by an external source.

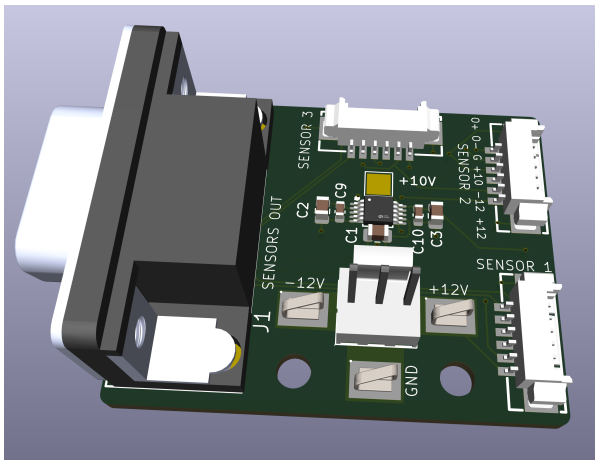


Figure 17: A render of the signal board.

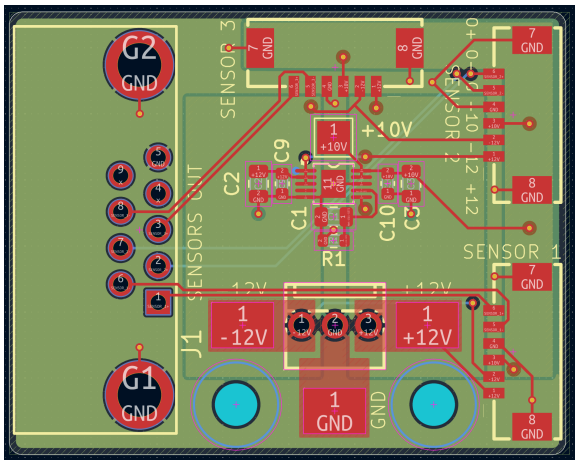


Figure 18: Signal board PCB.

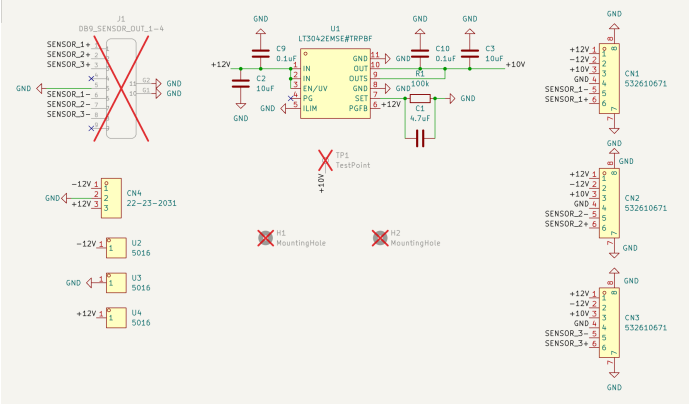


Figure 19: Signal board schematic.

This board was designed with a four-layer architecture (Fig. 18) due to the complexities of providing each connector with three separate voltages. A dedicated power plane is used to distribute all three voltages with low impedance. Each board has three channels, meaning two boards are necessary for the complete six-sensor design.

2.8 Coil Driver Boards

The engineering goal of the coil driver boards was to combine the current sourcing capability of power op-amps with the accuracy of precision op-amps to create a voltage-to-current feedback loop. The primary components involved are the TI OPA564 power op-amp, the INA849 ultra-low noise instrumentation amplifier, the OP2177 op-amp, and the AD8277 differential amplifier (Fig. 20).

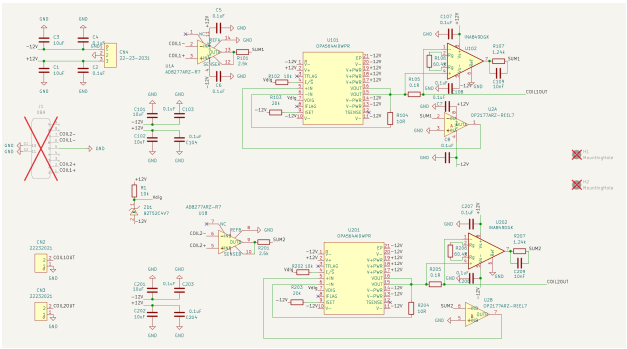


Figure 20: Coil board schematic.

The command voltage differential input from the controls computer DAC first goes through the AD8277 to take advantage of the IC's high common-mode rejection ratio (CMRR) and ground one end of the differential signal. The command voltage then combines with a feedback voltage obtained through the INA849 across a current sense resistor on the output of the power op-amp. Both of these voltages are fed into the inverting input of the OP2177 op-amp

whose output is connected directly to the non-inverting input of the OPA564 power op-amp. Because the non-inverting input of the OP2177 is grounded, it works to get its input to virtual ground by making the OPA564 power op-amp drive current through the current sense resistor until the output of the INA849 instrumentation amp is equal to the command voltage coming from the DAC. This is how the circuit as a whole converts the differential input into a current-based feedback loop that drives a consistent amount of current through the wires independent of wire temperature and therefore resistance (Fig. 21).

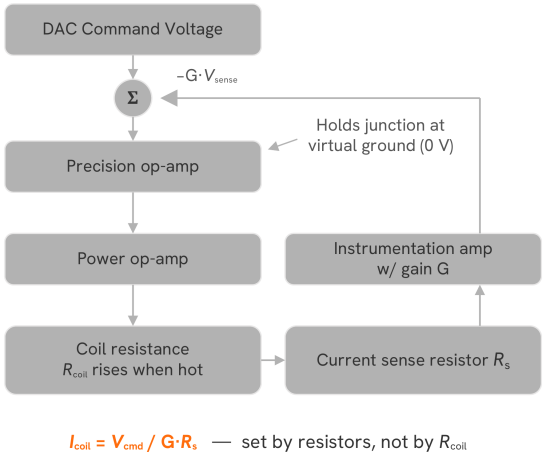


Figure 21: Block diagram of the current-based analog feedback loop. The precision op-amp holds the summing junction at virtual ground, so the coil current $I_{\text{coil}} = V_{\text{cmd}}/(GR_s)$ is set by the instrumentation amplifier gain G and the current sense resistor R_s rather than by the coil resistance R_{coil}, which rises as the coil heats.

The circuit also includes numerous decoupling capacitors for each IC. As per typical standards, each IC has one 100 nF capacitor placed right next to each of its supply pins, and the power op-amps also each have their own 10 μF bulk decoupling capacitors on each rail. Each board (Fig. 22 and Fig. 23) includes two channels, taking advantage of the dual packages offered for two of the ICs used, the OP2177 and the AD8277, variants of the OP1177 and AD8276 respectively.

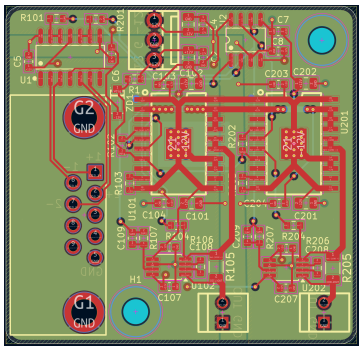


Figure 22: Coil board PCB. This is designed in a similar manner to the signal board PCB, with four-layer construction and dedicated power and ground planes.

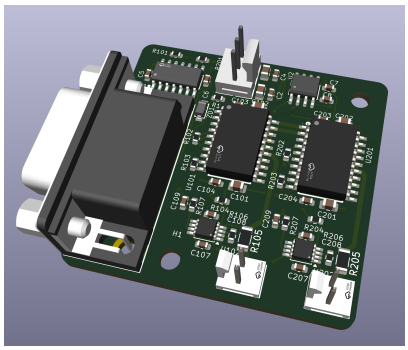


Figure 23: Coil board PCB render.

Due to the complex nature of this circuit, it was deemed necessary to simulate it in LTspice before fabrication. An identical single-channel circuit was built with SPICE models provided by TI and Analog Devices. The circuit takes a floating sine wave voltage input and returns a sine wave current, and was simulated at both 50 Hz and 5 kHz (Fig. 25 and Fig. 24). This model was used to test different combinations of gain resistors to arrive at the ideal ratio. A ratio of 2:1 was chosen, giving the circuit ±500 mA capability across the CyMAC DAC's ±10V range. This ratio is set by R1 and R3 in the LTspice diagram (Fig. 25).

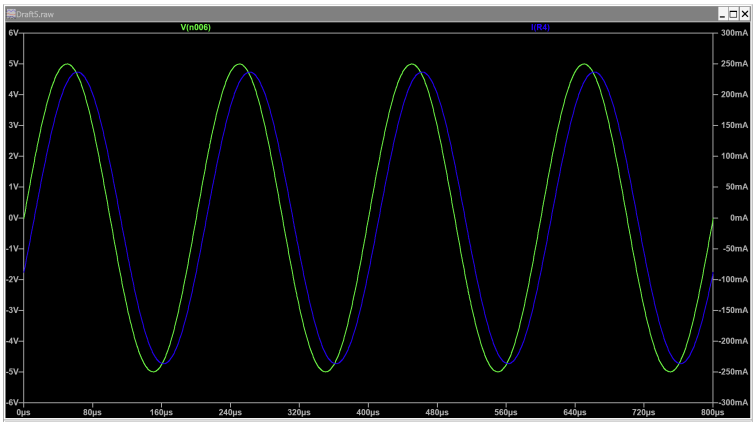


Figure 24: A 5 kHz trial simulation of the current driver circuit in LTspice illustrating the ∼15 μs delay between the command voltage and resulting current. This delay is determined by the resistance and inductive load of the coils the circuit is driving. In this simulation, the estimated values for a 6-inch (15 cm) diameter coil with 35 turns of 26 AWG wire were used: 1.8 Ω and 0.52 mH resistance and inductance, respectively.

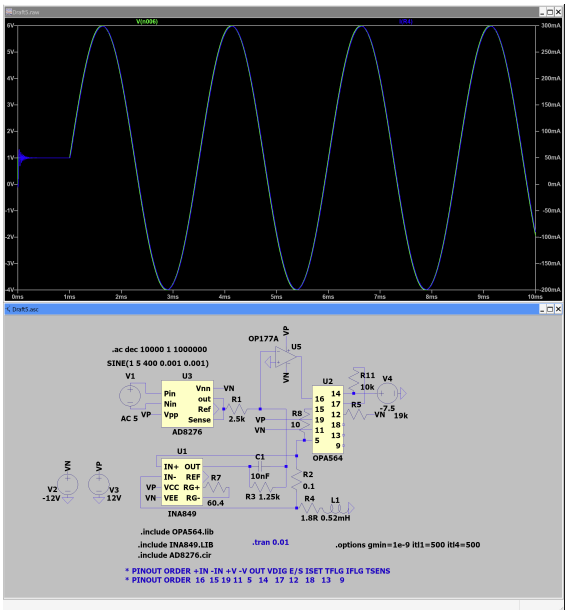


Figure 25: A 50 Hz simulation of the same circuit. The oscillations at the start are caused by LTspice's numerical models' difficulty in converging initially, likely caused by a poor SPICE model design of the OPA564 as I could not get it to work properly even when isolated with a DC voltage input.

2.9 CAD Design

The coil apparatus was designed to be 3D printed for easy assembly and testing (Fig. 26). The three Helmholtz coil pairs are arranged in a cubic layout, with six sensor PCBs mounted in the corners. The coils are held in place by a 3D printed base and support structure (Fig. 27).

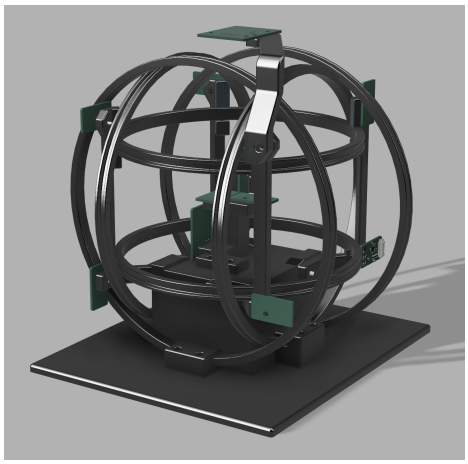


Figure 26: CAD model of the full 3D printed apparatus with the Helmholtz coils and sensor boards.

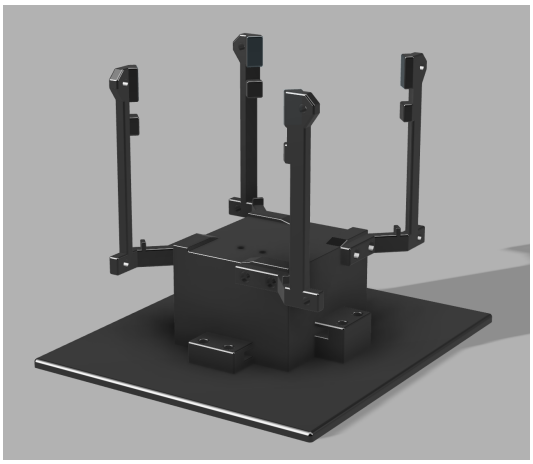


Figure 27: CAD model of the base and support structure without the coils.

2.10 Active Feedback Loop

The feedback loop was implemented on the CyMAC, which runs at a 65 kHz clock speed and allows Simulink-style loop creation. A proportional (P) loop was used with a custom frequency-dependent gain filter (Fig. 28), which applies narrow gain peaks at 60 Hz and its odd harmonics while leaving the gain unchanged at other frequencies.

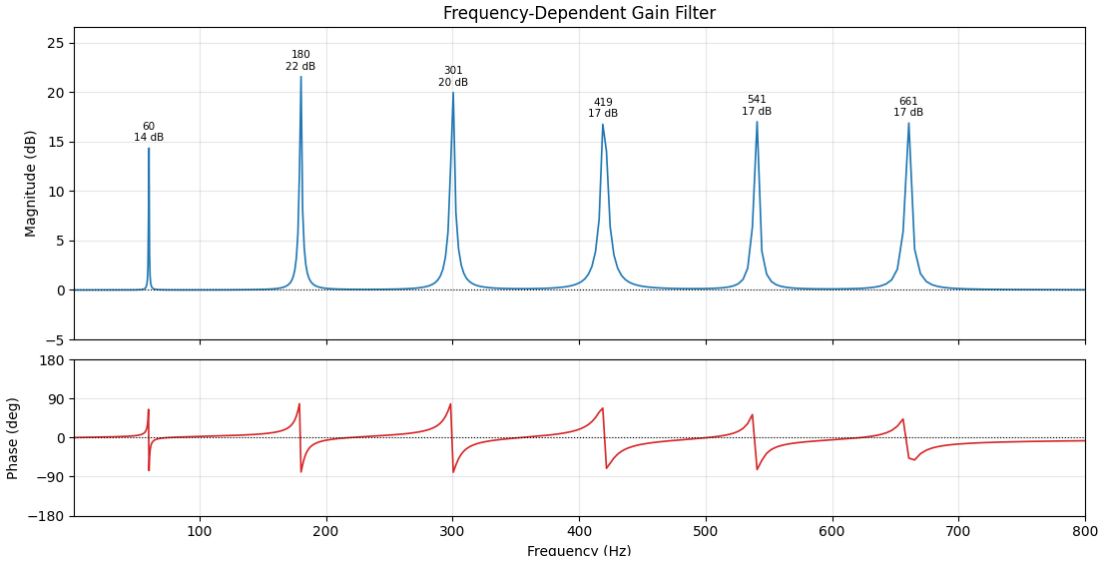


Figure 28: Frequency-dependent gain filter used in the P feedback loop. Narrow gain peaks of 14 to 22 dB are placed at 60 Hz and its odd harmonics up to 660 Hz, with 0 dB of gain elsewhere. The absence of even harmonics was attributed to the symmetry of mains electricity AC waveforms.

2.11 Experimental Setup

The stabilization system was tested on the x-axis, with a witness sensor at the center of the apparatus measuring the magnetic field. The exterior loop sensors were not used in this preliminary trial; rather, an additional witness sensor in the center was repurposed as a closed-loop sensor (Fig. 29). DE-9 ribbon cables were used to connect the system to the CyMAC (Fig. 30). While control of individual coils within each axis is possible with the hardware as designed, this trial was conducted with the same feedback voltage being sent to each coil on the x-axis due to time constraints. This method reduced the complexity of the trial by treating the coils as if they were wired in series.

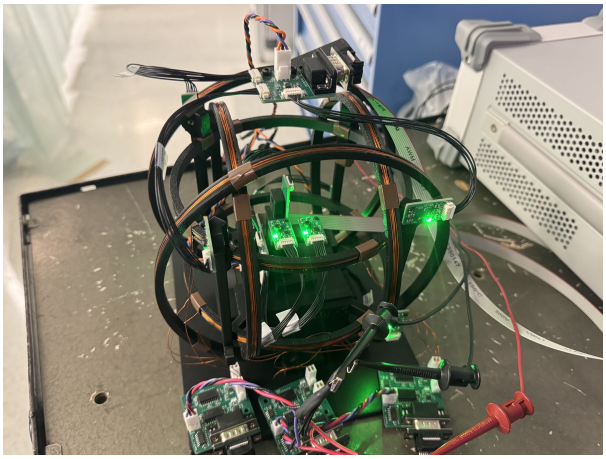


Figure 29: Witness and closed-loop sensor pictured at the center of the apparatus.



Figure 30: Complete system pictured with Rigol DP832A DC power supply and DE-9 cables to and from the CyMAC.

3 Results and Discussion

3.1 Ambient Field Suppression

The witness sensor measured the x-axis magnetic field with the feedback loop open (Fig. 31) and closed (Fig. 32). With the P-loop and frequency-dependent gain filter engaged, ambient lab noise was suppressed by 22, 19, and 20 dB at 60, 180, and 300 Hz, respectively (Fig. 33). Noise was also suppressed at 1 Hz from 6 $\mathrm{nT}/\sqrt{\mathrm{Hz}}$ down to a sensor-limited 4 $\mathrm{nT}/\sqrt{\mathrm{Hz}}$. The peaks near 38 and 76 Hz, which lie outside the filter bands, remain in the closed loop spectrum and are attributed to mechanical noise from the lab's air purification fans at 38.125 Hz and its harmonics.

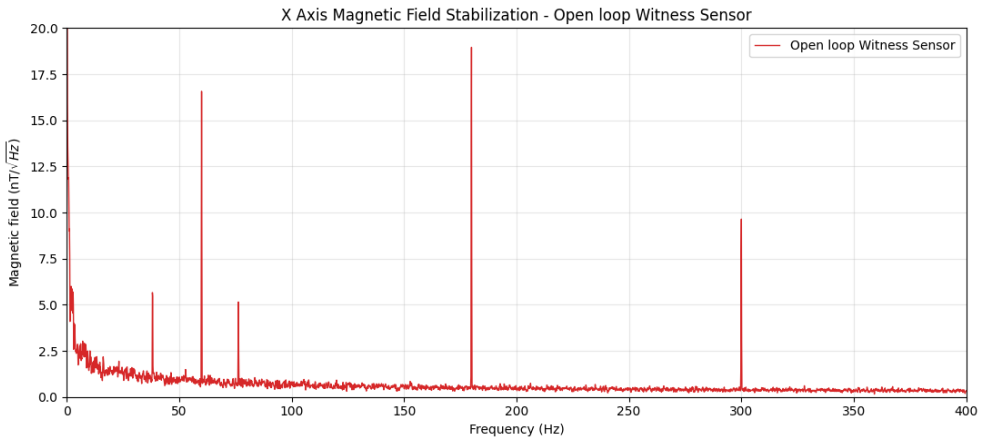


Figure 31: Open-loop amplitude spectral density of the x-axis magnetic field measured by the witness sensor.

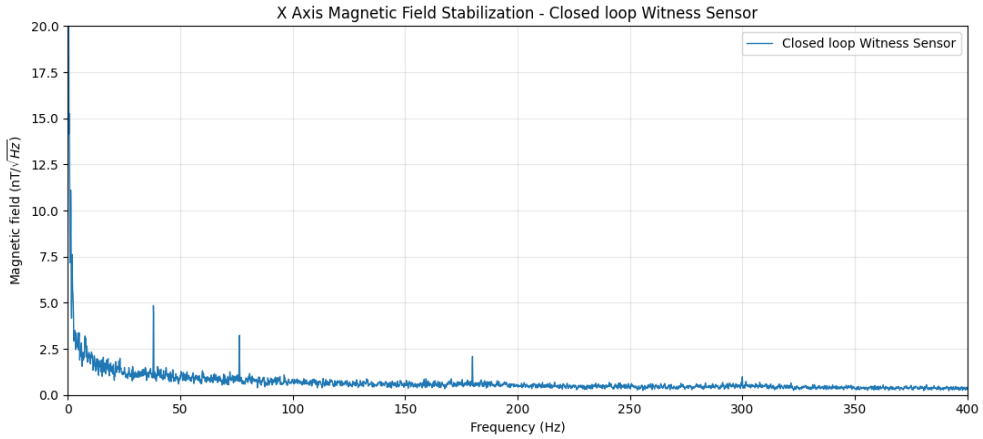


Figure 32: Closed-loop amplitude spectral density of the x-axis magnetic field measured by the witness sensor, with the frequency-dependent gain filter engaged.

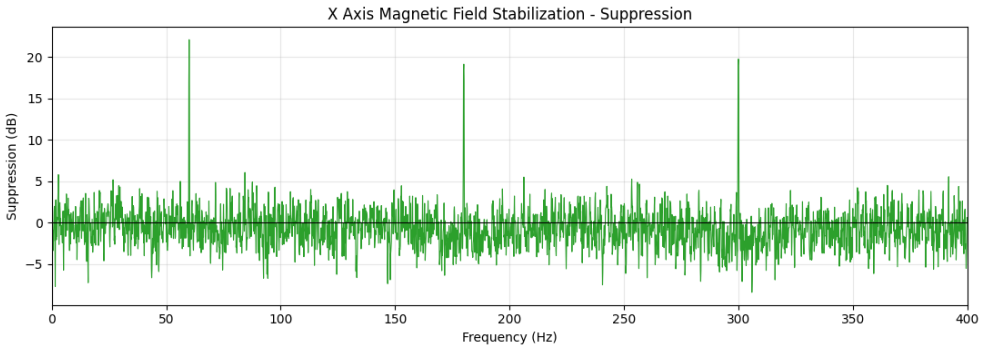


Figure 33: Suppression of the x-axis magnetic field noise with the feedback loop closed, relative to the open loop measurement.

3.2 Future Work

As mentioned in the methods, the initial trial's P-loop was closed with a sensor in the center of the apparatus rather than any of the exterior sensors; doing so in the required usage scenario would be impossible as the loop sensor's location would be occupied by the ^{87}Rb atoms. One of the first next steps in this project will involve designing a loop on the CyMAC capable of effective cancellation through the input of only exterior sensors. Additionally, both x-axis coils were driven by the same command voltage, leaving unused a degree of freedom the hardware supports, and the y and z axes were not tested due to time constraints. Running feedback on each of the 6 coils individually would not only allow for stabilization in all axes but also unlock control of the field's first spatial derivative, increasing the volume of space the system is capable of field-stabilizing.

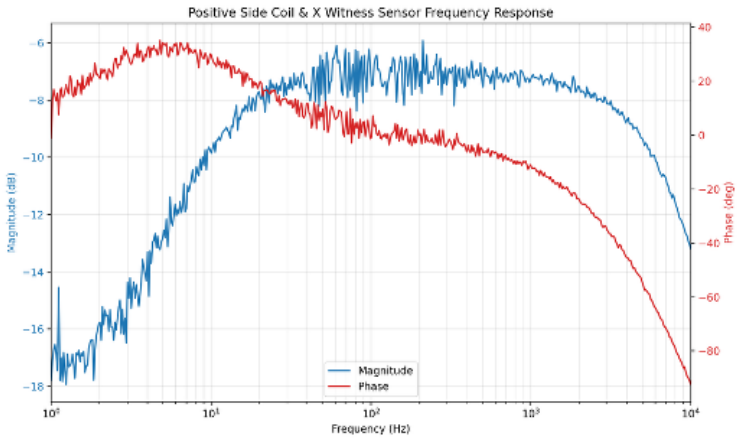


Figure 34: A swept sine taken on the x-axis witness sensor, driven through the x-axis coils. This measurement was taken on a Moku:Go.

The feedback P-loop used in the initial trial was rudimentary and could be significantly improved through fine-tuning of existing parameters and the inclusion of integral and derivative elements to form a complete PID loop. Doing so could yield increased suppression of noise such as the mechanical noise peaks at 38.125 Hz as well as the 60 Hz peaks and harmonics. Furthermore, no information from swept-sine measurements of the completed PCBs was taken into account during the creation of the loop (Fig. 34); additional work in integrating the hardware characteristics into the feedback filter would prove fruitful.

At the time of writing, many details of the RbQ project are still being finalized. As a result, the specifications of the final apparatus have not yet been determined. Most notably, it has not yet been decided if the coils and sensors will be positioned inside or outside the ultra-high vacuum chamber. This decision will have profound implications on the hardware design of the system: if it is to be placed outside the vacuum chamber, the coils will have to be significantly larger, and the electronics driving them will be required to deal with significantly higher currents and load inductance. If the system components are to be placed in the vacuum chamber, each part will have to be redesigned with ultra-high vacuum compatibility in mind.

Lastly, while the exact field stability requirements for RbQ have not yet been determined, they will very likely be at least an order of magnitude below the noise floor of the TMR sensors used in this project's initial trials. Due to long lead times, it was not possible to obtain a true ultra-low noise magnetic field sensor within the timeframe of this fellowship. Future work will be required to integrate far more sensitive sensors into the current system architecture. While this is a significant change, I believe much of the project's developments so far will be compatible with higher sensitivity sensors after relevant adjustments.

3.3 Conclusion

This project demonstrated the feasibility of active magnetic field stabilization as applied to the RbQ experiment. After characterizing the 1051Z AMR and ALT021 TMR sensors, the TMR sensor was selected for its high sensitivity and lack of an SR pulse requirement. Three custom PCBs were designed, simulated, and fabricated to implement the full sensing and feedback loop, and a 3D printed Helmholtz coil apparatus was built to house them. In an initial single-axis trial, a simple P-loop with a frequency-dependent gain filter suppressed ambient lab noise by 22, 19, and 20 dB at 60, 180, and 300 Hz, respectively, and reduced the noise at 1 Hz to the sensor-limited floor of $4\,\mathrm{nT}/\sqrt{\mathrm{Hz}}$. While significant work remains before the system can be integrated into RbQ, these results show that the current architecture provides a solid foundation for future development.

4 Acknowledgements

I would like to thank my mentors, Jeffrey Wack and Lee McCuller, for their guidance and support throughout this project. I would also like to thank the rest of the McCuller lab for their help in the lab, as well as my fellow LIGO SURF students for making this summer a great experience. This work was supported by the National Science Foundation (NSF), the LIGO Laboratory Summer Undergraduate Research Fellowship program (LIGO SURF), and the California Institute of Technology Student-Faculty Programs.

References

[1]L. McCuller, "Quantum optimal stochastic-signal searches: seeding "post-squeezing" quantum metrology for fundamental physics", Seed proposal, California Institute of Technology (2024).

[2]M. Fleischhauer and M. D. Lukin, "Dark-state polaritons in electromagnetically induced transparency", Physical Review Letters **84**, 5094–5097 (2000).

[3]J. Dilley, P. Nisbet-Jones, B. W. Shore, and A. Kuhn, "Single-photon absorption in coupled atom-cavity systems", Physical Review A **85**, 023834 (2012).

[4]R. Loughman, *2025 LIGO SURF final report: numerical simulation of quantum enhanced interferometer readout*, Technical Note LIGO-T2500249v1-G, Hamilton College (LIGO Laboratory, California Institute of Technology and Massachusetts Institute of Technology, July 2025).

[5]S. M. Vermeulen, T. Cullen, D. Grass, I. A. O. MacMillan, A. J. Ramirez, J. Wack, B. Korzh, V. S. H. Lee, K. M. Zurek, C. Stoughton, and L. McCuller, "Photon-counting interferometry to detect geontropic space-time fluctuations with GQuEST", Physical Review X **15**, 011034 (2025).

[6]B. Merkel, K. Thirumalai, J. E. Tarlton, V. M. Schäfer, C. J. Ballance, T. P. Harty, and D. M. Lucas, "Magnetic field stabilization system for atomic physics experiments", Review of Scientific Instruments **90**, 044706 (2019).

[7]Honeywell Sensor Products, *HMC1051Z/HMC1052: 1 and 2-axis magnetic sensors*, Data sheet, Form 900296, Rev. A, (2002) `https://arauzsl.com/wp-content/productos/sensores/HO_MAG_HMC10511052.pdf` (visited on 09/13/2026).

[8]NVE Corporation, *ALT-series TMR analog magnetometer sensors*, Data sheet, SB-00-102, Rev. O, (Aug. 2026) `https://www.nve.com/Downloads/ALTxxx-10.pdf` (visited on 09/13/2026).

[9]R. Bork, J. Hanks, D. Barker, J. Betzwieser, J. Rollins, K. Thorne, and E. von Reis, "advligorts: the Advanced LIGO real-time digital control and data acquisition system", SoftwareX **13**, 100658 (2021).